

NANO EXPRESS

Open Access



Composition-Tunable Optical Properties of $\text{Zn}_x\text{Cd}_{(1-x)}\text{S}$ Quantum Dot–Carboxymethylcellulose Conjugates: Towards One-Pot Green Synthesis of Multifunctional Nanoplatforms for Biomedical and Environmental Applications

Alexandra A. P. Mansur¹, Herman S. Mansur^{1,3*}, Anderson J. Caires¹, Rafael L. Mansur¹ and Luiz C. Oliveira²

Abstract

Quantum dots (QDs) are colloidal semiconductor nanocrystals with unique properties that can be engineered by controlling the nanoparticle size and chemical composition by doping and alloying strategies. However, due to their potential toxicity, augmenting their biocompatibility is yet a challenge for expanding to several biomedical and environmentally friendly applications. Thus, the main goal of this study was to develop composition-tunable and biocompatible $\text{Zn}_x\text{Cd}_{1-x}\text{S}$ QDs using carboxymethylcellulose polysaccharide as direct capping ligand via green colloidal aqueous route at neutral pH and at room temperature for potential biomedical and environmental applications. The ternary alloyed QDs were extensively characterized using UV–vis spectroscopy, photoluminescence spectroscopy (PL), transmission electron microscopy (TEM), X-ray diffraction (XRD), electron energy loss spectroscopy (EELS), and X-ray photoelectrons spectroscopy (XPS). The results indicated that $\text{Zn}_x\text{Cd}_{(1-x)}\text{S}$ QDs were surface stabilized by carboxymethylcellulose biopolymer with spherical morphology for all composition of alloys and narrow sizes distributions ranging from 4 to 5 nm. The XRD results indicated that monophasic ternary alloyed $\text{Zn}_x\text{Cd}_{1-x}\text{S}$ nanocrystals were produced with homogenous composition of the core as evidenced by EELS and XPS analyses. In addition, the absorption and emission optical properties of $\text{Zn}_x\text{Cd}_{1-x}\text{S}$ QDs were red shifted with increasing the amount of Cd^{2+} in the alloyed nanocrystals, which have also increased the quantum yield compared to pure CdS and ZnS nanoparticles. These properties of alloyed nanomaterials were interpreted based on empirical model of Vegard's law and chemical bond model (CBM). As a proof of concept, these alloyed-QD conjugates were tested for biomedical and environmental applications. The results demonstrated that they were non-toxic and effective fluorophores for bioimaging live HEK293T cells (human embryonic kidney cells) using confocal laser scanning fluorescence microscopy. Moreover, these conjugates presented photocatalytic activity for photodegradation of methylene blue used as model

(Continued on next page)

* Correspondence: hmansur@demet.ufmg.br

¹Center of Nanoscience, Nanotechnology and Innovation - CeNano(2)I, Department of Metallurgical and Materials Engineering, Universidade Federal de Minas Gerais—UFMG, Belo Horizonte, Brazil

³Federal University of Minas Gerais, Av. Antônio Carlos, 6627 – Escola de Engenharia, Bloco 2 – Sala 2233, Belo Horizonte, MG 31.270-901, Brazil

Full list of author information is available at the end of the article

(Continued from previous page)

organic industrial pollutant in water. Hence, composition-tunable optical properties of ternary $\text{Zn}_x\text{Cd}_{1-x}\text{S}$ ($x = 0-1$) fluorescent alloyed QDs was achieved using a facile eco-friendly aqueous processing route, which can offer promising alternatives for developing innovative nanomaterials for applications in nanomedicine and environmental science and technology.

Keywords: Semiconductor quantum dot nanoparticles, Nanomaterials, Semiconductor-biopolymer interfaces, Nanophotocatalyst, Core-shell nanostructures

Background

Traditionally, alloys have been used for several centuries to create new materials with improved mechanical, structural, thermal, electrical properties leading to the development of high-performance materials, which cannot be achieved with each component separately. However, only very recently the interest in nanoalloys (also referred to as alloy nanoclusters or alloy nanoparticles) arises, as they constitute a new type of advanced nanoscale materials, which can have unique properties very distinct from those of individual atoms and molecules or original bulk matter [1–4]. One of the major reasons for interest in alloy nanoparticles is the fact that their chemical and physical properties may be tuned by varying the composition and atomic ordering as well as the dimension of the clusters [4, 5]. Besides the metal-based nanomaterial alloys, nano-sized semiconductor nanocrystals (referred to as quantum dots, QDs) have increasingly called the attention of the scientists, researchers, and manufacturers because of their broad range of potential applications in electronics, optics, magnetic, sensors, biosensors, and biomedical fields [6–11]. In that sense, quantum dots based on metal chalcogenide alloys, mostly of group II–VI semiconductors (type MX , $\text{M} = \text{Cd}, \text{Zn}, \text{Pb}$; $\text{X} = \text{Te}, \text{Se}, \text{S}$), are currently under intensive study in many research fields such as in optoelectronics, high-density memory, quantum-dot lasers, and lately for biosensing and biolabeling because they exhibit tunable optical properties (i.e., bandgap energy structure) by adjusting the chemical composition and size [5, 7, 12–15]. Since the bandgap engineering of ternary and quaternary alloyed QDs can be achieved via controlling their composition (relative constituent stoichiometry) in addition to their sizes and internal structures, it is therefore feasible to design and tune their optical properties, which are not readily viable to binary QDs [16–19]. This can be achieved by creating a solid solution (i.e., an alloy) of two semiconductors with different energy gaps, where an increase in the bandgap energy is generally observed with increasing the concentration of the wider bandgap semiconductor, either with cation (i.e., metal constituent) or anion (i.e., chalcogenide constituent) alloyed QDs [20, 21]. Nonetheless, the development of QDs based on

Zn-Cd-S alloys using one-pot “greener” aqueous processes with biocompatible ligands are narrowly reported in the literature, where the large majority of studies report the production of QDs at high temperatures by organometallic routes, microwave-assisted synthesis, and using toxic organic solvents [15, 17, 18, 21–25]. High-temperature decomposition methods based on trioctylphosphine oxide (TOPO), commonly used as capping ligand for improved quantum yields, results in hydrophobic QDs insoluble in aqueous medium. However, biological and medical applications require QDs that are water-soluble at physiological conditions, biocompatible, and functionalized with biomolecules for targeting purposes. Hence, the development of novel strategies of surface functionalization and bioconjugation remains an important challenge. Yet, no report was found in the consulted literature addressing the synthesis of $\text{Zn}_x\text{Cd}_{1-x}\text{S}$ QDs functionalized with biopolymer ligands based on cellulose derivatives for multiple potential purposes, including cell bioimaging and photocatalytic activity for the degradation of organic dye pollutants.

Thus, herein, we report the synthesis and comprehensive characterization of novel ternary alloyed $\text{Zn}_x\text{Cd}_{1-x}\text{S}$ QDs ($x = 0 \rightarrow 1$) with composition-tunable optical properties using carboxymethylcellulose as a biocompatible and eco-friendly capping ligand produced directly by means of a single-step green colloidal process in aqueous media at room temperature. They proved to be suitable nanoplatforams for live cell bioimaging or heterogeneous photocatalysis of methylene blue organic dye.

Methods

Materials

All of the reagents and precursors, including zinc chloride (Sigma-Aldrich, USA, $\geq 98\%$, ZnCl_2), cadmium perchlorate hydrate (Aldrich, USA, $\text{Cd}(\text{ClO}_4)_2 \cdot 6\text{H}_2\text{O}$), and sodium sulfide hydrate (Synth, Brazil, $>98\%$, $\text{Na}_2\text{S} \cdot 9\text{H}_2\text{O}$) were used as received. Carboxymethylcellulose sodium salt (CMC_{el}, Fluka Chemical, USA), degree of substitution (DS) 0.84 and medium viscosity (870 mPa s, 2% in H_2O) was used as capping ligand. Deionized water (DI water, Millipore SimplicityTM) with a resistivity of 18 M Ω cm was used to prepare the solutions and the procedures were performed at room temperature (RT, $23 \pm 2^\circ\text{C}$), unless specified otherwise.

Synthesis of Quantum Dot Conjugates— $\text{Zn}_x\text{Cd}_{1-x}\text{S}/\text{CMCcl}$

CMCcl solution (1% w/v) was prepared by adding sodium carboxymethylcellulose powder (0.5 g) to a 50 mL of water and stirring at room temperature until complete solubilization occurred. For controlling the molar ratios of cations, premixed Zn^{2+} and Cd^{2+} solutions were prepared from the individual stock solutions (ZnCl_2 and $\text{Cd}(\text{ClO}_4)_2 \cdot 6\text{H}_2\text{O}$) at $1 \times 10^{-3} \text{ mol L}^{-1}$ total cation concentration (M) but with $\text{Zn}^{2+}:\text{Cd}^{2+}$ molar ratios of 100:0 ($x = 1.0$), 75:25 ($x = 0.75$), 50:50 ($x = 0.50$), 25:75 ($x = 0.25$), and 0:100 ($x = 0$).

$\text{Zn}_x\text{Cd}_{1-x}\text{S}$ nanoparticles were synthesized via an aqueous route at room temperature as follows: 2 mL of CMCcl solution and 45 mL of deionized water were added to a flask. The pH was measured and it was close to neutral (pH ~7.0). Under magnetic stirring, 20.0 mL of the metal precursor solution ($1 \times 10^{-3} \text{ mol L}^{-1}$) at the $\text{Zn}^{2+}:\text{Cd}^{2+}$ different molar ratios and 4.0 mL of the sulfide source solution ($\text{Na}_2\text{S} \cdot 9\text{H}_2\text{O}$, $1.0 \times 10^{-2} \text{ mol L}^{-1}$) were added to the flask (the $\text{S}^{2-}:\text{M}^{2+}$ molar ratio was kept at 2:1, i.e., excess of sulfide) and stirred for 10 min. The QDs colloidal dispersions produced were stable and homogeneous. ZnS dispersion was colorless while CdS dispersion was light yellow. The dispersions of ternary $\text{Zn}_x\text{Cd}_{1-x}\text{S}$ nanoparticles exhibit colors between clear and light yellow with continuous color gradient as a function of the $\text{Zn}^{2+}:\text{Cd}^{2+}$ molar ratio.

These colloidal dispersions were concentrated and purified using an Amicon® Ultra Filter (Millipore) with a 100,000 molecular mass (M_w) cut-off cellulose membrane. Centrifugation was conducted and, after the first cycle, the QDs were washed 4 times with DI water. Centrifugal forces caused the removal of excess reagents through the membrane into a filtrate vial. After purification, the samples were stored at RT until further use.

Physicochemical Characterization of Quantum Dot Conjugates

Ultraviolet–visible (UV–vis) spectroscopy measurements were performed using Perkin-Elmer, Inc. (USA) equipment (Lambda EZ-210) in transmission mode with samples in a quartz cuvette over a wavelength range between 600 and 190 nm. All of the experiments were conducted in triplicate ($n = 3$) unless specifically noted, and the data were presented as the mean \pm standard deviation.

The photoluminescence spectroscopy (PL) of the $\text{Zn}_x\text{Cd}_{1-x}\text{S}/\text{CMCcl}$ conjugates was performed based on spectra acquired at RT using a violet diode laser module at $\lambda_{\text{exc}} = 405 \text{ nm}$ (150-mW, Roithner Laser Technik, Germany) coupled to a USB4000 VIS-NIR spectrophotometer (Ocean Optics, Inc., USA). All of the tests were performed using a minimum of four repetitions ($n \geq 4$). Quantum yield (QY) was measured according to the procedure using

Rhodamine 6G (Sigma, USA) in ethanol as the standard at $\lambda_{\text{excitation}} = 405 \text{ nm}$ [26]. Nanostructural characterization of the QDs was based on the images and electron diffraction patterns (ED) using Tecnai G2-20-FEI (FEI Company, USA) transmission electron microscope (TEM) at an accelerating voltage of 200 kV. In all of the TEM analyses, the samples were prepared by placing a drop of a dilute QD suspension onto carbon-coated copper grids (Electron Microscopy Sciences, USA) and allowing them to dry at room temperature overnight. The QD size and size-distribution data were obtained based on the TEM images by measuring at least 150 randomly selected nanoparticles using image processing program (ImageJ, version 1.50, public domain, National Institutes of Health) [27].

X-ray diffraction (XRD) patterns were recorded using PANalytical (UK) Empyrean diffractometer ($\text{Cu-K}\alpha$ radiation with $\lambda = 1.5406 \text{ \AA}$). Measurements were performed in the 2θ range from 3° to 70° with steps of 0.06° . For the sample preparation, concentrated colloidal QD dispersions were dropped onto glass slides and oven dried at $40 \pm 1^\circ\text{C}$ for 12 h.

Energy-filtered transmission electron microscopy (EFTEM) with low-loss electron energy-loss spectroscopy (EELS) was performed by using Tecnai G20 TEM operating at 200 kV accelerating voltage and equipped with GATAN GIF energy imaging filter. The cadmium composition map was obtained using the Cd M edge at 404 eV, and the Zn composition map was obtained using the Zn L edge at 1020 eV, using similar sample preparation procedure of TEM analysis.

X-ray photoelectron spectroscopy (XPS) analysis was performed using Mg- $\text{K}\alpha$ as the excitation source (Amicus spectrometer, Shimadzu, Japan). All peak positions were corrected based on C 1s binding energy (284.6 eV). For sample preparation, concentrated QD colloidal medium was dropped onto glass slides and dried in a vacuum desiccator at RT for 48 h.

Dynamic light scattering (DLS) and zeta potential (ZP) analyses were performed using ZetaPlus instrument (Brookhaven Instruments Corporation, 35-mW red diode laser light, wavelength $\lambda = 660 \text{ nm}$) with a minimum of ten replicates. The ZP measurements were performed at $25.0^\circ\text{C} \pm 2^\circ\text{C}$ under the Smoluchowski approximation method. For the DLS measurements, the colloidal solutions of QDs were filtered three times through a $0.45\text{-}\mu\text{m}$ aqueous syringe filter (Millex LCR 25 mm, Millipore).

Biological Characterization of QD Conjugates

Evaluation of Cytotoxicity by MTT Cell Viability Assay

MTT (3-(4,5-dimethylthiazol-2-yl) 2,5-diphenyl tetrazolium bromide) experiments were performed to evaluate the toxicity of QDs dispersions. MTT assays were conducted according to ISO 10993-5:2009 (Biological evaluation of medical devices: Tests for in vitro cytotoxicity)

using kidney cell line of a human embryonic culture (HEK293T). HEK293T cells were kindly provided by Prof. M.F Leite (Department of Physiology and Biophysics, UFMG), and they were cultured in DMEM with 10% FBS, penicillin G sodium (10 units mL⁻¹), streptomycin sulfate (10 mg mL⁻¹), and amphotericin-b (0.025 mg mL⁻¹), all from Gibco BRL (NY, USA), in a humidified atmosphere of 5% CO₂ at 37 °C.

HEK293T cells on passage 68 were plated (3×10^4 cells/well) in 96-well plates. Cell populations were synchronized in serum-free media for 24 h. After that, the media volume was suctioned and replaced with DMEM media containing 10% FBS for 24 h. The samples of CdS, ZnS, and Zn_{0.50}Cd_{0.50}S QDs colloidal solutions were added to individual wells at final concentrations of 10 nM. For MTT assay, control samples were designed as follows: control group (cell culture with DMEM medium); positive control (1.0% Triton X-100, Sigma-Aldrich, USA); and negative control (chips of sterile polypropylene Eppendorf, 1 mg mL⁻¹, Eppendorf, Germany). After 120 h, all media were aspirated and replaced with 60 µL of culture media containing serum to each well. MTT (5 mg mL⁻¹, Sigma-Aldrich, USA) was added to each well and incubated for 4 h in an oven at 37 °C and 5% CO₂. Next, 40 µL SDS (Sigma-Aldrich, USA) solution/4% HCl was placed in each well and incubated for 16 h in an oven at 37 °C and 5% CO₂. Then, 100 µL was removed from each well and transferred to a 96-well plate. The absorbance was measured at 595 nm on iMark™ Microplate Absorbance Reader (Bio-Rad) with a 595-nm filter. Percentage cell viability was calculated according to Eq. 1. The values of the controls (wells with cells and no samples) were set to 100% cell viability.

$$\text{Cell viability} = \frac{(\text{Absorbance of sample and cells})}{(\text{Absorbance of control})} \times 100 \% \quad (1)$$

Cellular Uptake of QD Conjugates by Laser Scanning Confocal Microscopy

The evaluation of the QD conjugates as fluorescent biological probes was performed using confocal laser scanning microscopy after exposing ZnS and Zn_{0.50}Cd_{0.50}S QDs to HEK293T cells. For the cellular internalization evaluation, HEK293T cells on passage 68 were plated (5×10^4 cells per well) in 24-well plate. The cells were incubated for 4 days in 5% CO₂ at 37 °C and synchronized for 24 h, and the ZnS and Zn_{0.50}Cd_{0.50}S colloidal suspensions with the medium solution (DMEM) at final concentration of 500 nM were added to the cells. Next, the cells were incubated in 5% CO₂ at 37 °C for 1 h and washed with phosphate buffered saline (PBS, Gibco, Brazil). In the sequence, the cells were fixed with paraformaldehyde (4%)

for 30 min, washed three times with PBS, and cover slips were mounted with Hydromount (Fisher Scientific Ltd., UK) for posterior analysis in confocal laser scanning fluorescence microscopy (Zeiss LSM Meta 510, Carl Zeiss; excitation 488 nm argon laser; emission filter 505–530 nm). For the control, cells were incubated with only in the original medium with 10% FBS (autofluorescence).

Photocatalytic Activity of QD Conjugates for Environmental Applications

The photocatalytic activities of the ZnS and Zn_{0.50}Cd_{0.50} conjugates were evaluated via the photocatalytic degradation of molecule methylene blue (MB) as model organic pollutant molecule under ultraviolet (UV) light irradiation.

The experiments were performed at room temperature using 15 mL of a solution of MB (20 mg L⁻¹) containing 0.1 mL of each conjugate catalyst under mechanic stirring (330 rpm) and a mercury lamp radiation source (15 W, at $\lambda = 254$ nm). At certain time intervals, an aliquot of the material was collected and analyzed by UV-vis spectroscopy (Shimadzu-UV-1601 PC) to detect the dye concentration based on Beer–Lambert curves established to correlate the absorbance with the dye concentration at the characteristic maximum absorption wavelength ($\lambda = 664$ nm). The degradation efficiency was calculated using Eq. 2 where “C₀” is the initial concentration of the dye ($t = 0$) and “C” is the concentration of MB at a given time of radiation exposure (t). A control experiment was performed without the presence of the catalytic conjugates.

$$\begin{aligned} \text{Degradation efficiency (\%)} \\ = [(C_0 - C)/C_0] \times 100 \% \end{aligned} \quad (2)$$

Results and Discussion

Physicochemical Characterization of Quantum Dot Conjugates

Figure 1A shows de UV-vis spectra for Zn_xCd_{1-x}S ($x = 1.0, 0.75, 0.50, 0.25$, and 0) series. ZnS nanoparticles (Fig. 1A(a)) presents a sharp absorption edge at approximately 290 nm associated with the first excitonic transition indicating nucleation and growth of ZnS ($x = 1$) nanoparticles, blue shifted from the bulk value at 343 nm [28] due to the “quantum confinement regime.” Analogously, CdS ($x = 0$) colloidal suspension (Fig. 1A(e)) presented a broad absorption band from 430 to 470 nm, blue shifted when compared with the original bulk value ($\lambda = 512$ nm, [28]) indicating the formation of CdS QDs. The optical absorption spectra of Zn_xCd_{1-x}S ternary systems show a systematic red shift associated with the changes in the absorption onset of the S₀ → S₁ transitions as the Cd content increases which originates from the wider bandgap ZnS ($E_g =$

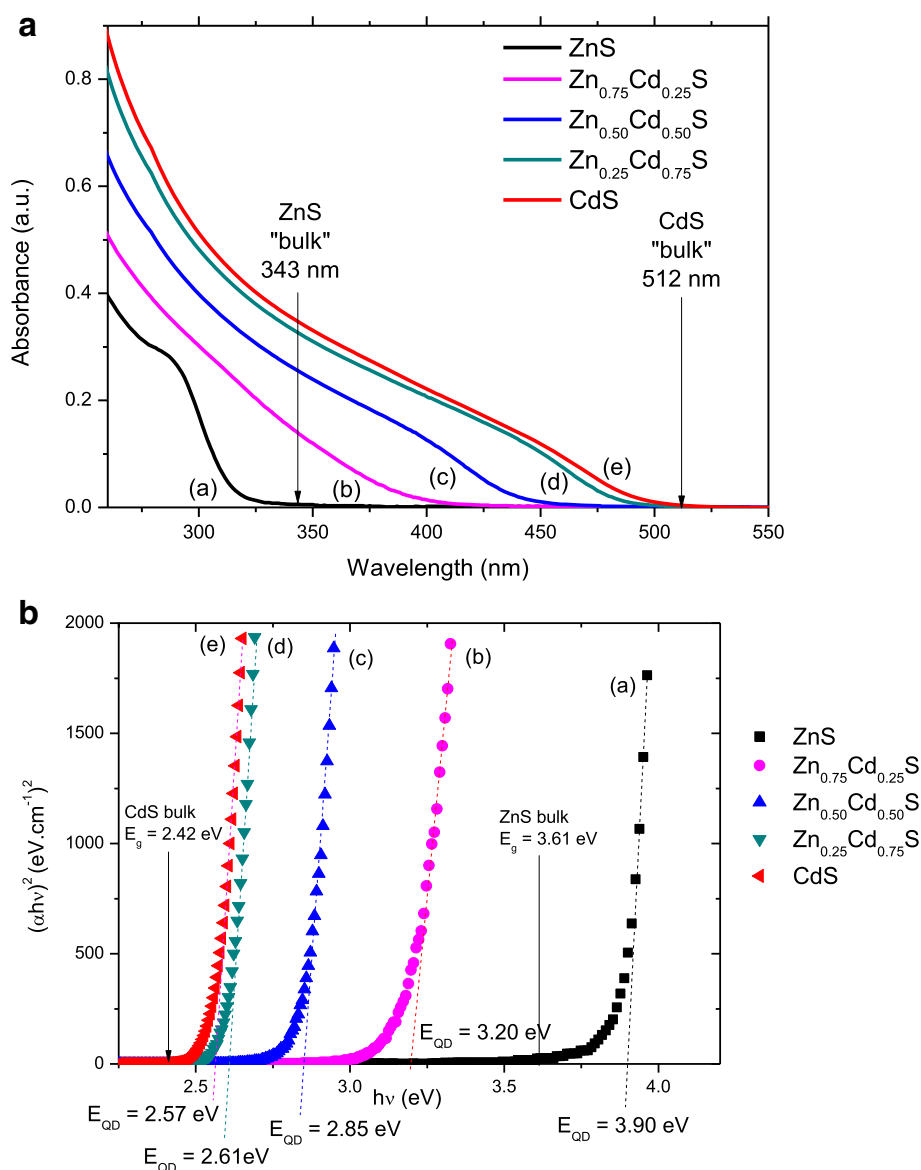


Fig. 1 UV-visible and optical absorption spectroscopy of conjugates. **a** UV-vis absorption spectra and **b** optical absorption spectra (relation) for ZnS (a), Zn_{0.75}Cd_{0.25}S (b), Zn_{0.50}Cd_{0.50}S (c), Zn_{0.25}Cd_{0.75}S (d), and CdS (e)

3.61 eV) relative to the narrower bandgap CdS ($E_g = 2.42$ eV) [28].

Bandgap values for the prepared metal sulfide QDs (E_{QD}) at different proportions of [Zn,Cd]:S were extracted from the UV-vis absorbance curves using the “TAUC relation” (Fig. 1B). The estimated E_{QD} values are 3.90, 3.20, 2.85, 2.61, and 2.57 eV for ZnS, Zn_{0.75}Cd_{0.25}S, Zn_{0.50}Cd_{0.50}S, Zn_{0.25}Cd_{0.75}S, and CdS, respectively. Therefore, the tunable bandgap effect was indeed verified, as the excitonic transitions for the Zn_xCd_{1-x}S ternary solid solutions (Fig. 1A (b–d)) continuously red shifted (i.e., shifted to lower energy) with increasing the amount of Cd²⁺, which demonstrated the formation of Zn_xCd_{1-x}S nanoalloys.

Typical room-temperature PL spectra of the Zn_xCd_{1-x}S nanoparticles stabilized by CMCel are presented in Fig. 2A. The Zn_xCd_{1-x}S QDs showed multi-colored light emissions arising predominantly from defect activated photoluminescence. That means, lattice point defects (vacancies, V, and interstitials atoms, I) act as efficient traps for electrons, holes, and exciton charge carriers, leading to radiative recombination at energies lower than the band-to-band optical transition (i.e., offering non-radiative pathways) [29, 30]. As previously reported [31, 32], due to the small size of QDs and the intrinsic lattice point defects introduced by the synthesis at room temperature and aqueous routes, band edge (excitonic) luminescence was not observed and

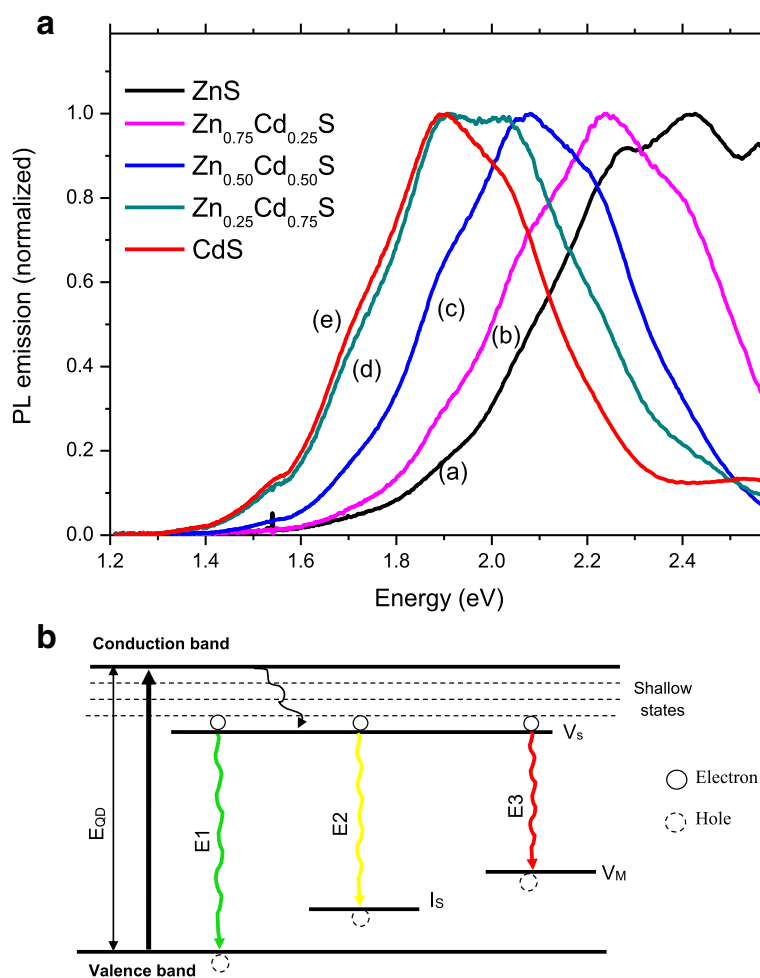


Fig. 2 Photoluminescence spectroscopy of conjugates. **a** PL emission spectra for Zn_xCd_{1-x}S ($x = 1.0$ (a), 0.75 (b), 0.50 (c), 0.25 (d), and 0 (e)). **b** The energy band structure suggested for three main emissions of alloyed Zn_xCd_{1-x}S quantum dots

the QYs were typically $\leq 2.0\%$ (1.0% for ZnS; 1.8% for Zn_{0.50}Cd_{0.50}S; 0.2% for CdS).

The occurrence, population, and depths of the traps determine the pathway that the electron–hole pairs (i.e., exciton, e^-/h^+) generated by irradiation will follow during emission. Considering the synthesis process developed in this work, using the stoichiometric molar ratio of $M^{2+}:S^{2-} = 1:2$ (i.e., higher sulfide to cation ratio), the occurrence of vacancies of metals (V_M : V_{Cd} or V_{Zn}) and sulfur at interstitial sites at lattice (I_S) are expected. Moreover, the strong interaction between the metallic cations and the anionic carboxylate species from CMCel, which are fully deprotonated at the pH of synthesis ($pK_a = 4.8$, $R-COOH \rightarrow R-COO^-$) can cause the formation of vacancies of sulfur (V_S) at the QD surface. Thus, considering the combination of the types of point defects (V_M , V_{Cd} , V_{Zn} , and I_S) and the similarity of the emission curves for Zn_xCd_{1-x}S, three main radiative emissions were observed in the nanoparticles, which were assigned

to the energy band diagram depicted in Fig. 2B and summarized in Table 1, supported by the literature [33–37].

First, there is a non-radiative pathway from valence band and energy level of V_S due to shallow trap states. In the sequence, the emission E1 can be associated with transitions involving sulfur vacancies (V_S) and valence band (V_B). Emission E2 can be assigned to the recombination of trapped electrons at V_S and holes trapped at interstitial metal (I_S) point defects and E3 is attributed to the recombination between vacancy trap states (V_S-V_M). The minor emission bands at higher wavelengths can be assigned to surface defects [33, 35]. Despite the nature of the emission, peaks in the PL spectra shifted to lower energy with the increase of Cd molar ratio in the QDs demonstrated the composition-tunable emission effect of nanoalloys. These values of red shift observed in the PL spectroscopy support the results of previous sections, and they are further strong evidence of the formation of alloyed nanocrystals.

Table 1 Summary of types and energies of $\text{Zn}_x\text{Cd}_{1-x}\text{S}$ QD emissions

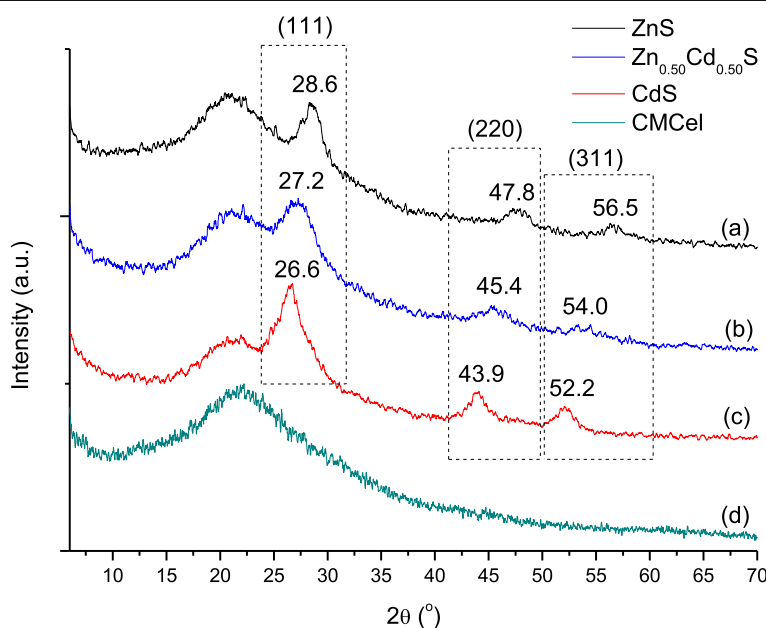
Emission		ZnS	$\text{Zn}_{0.75}\text{Cd}_{0.25}\text{S}$	$\text{Zn}_{0.50}\text{Cd}_{0.50}\text{S}$	$\text{Zn}_{0.25}\text{Cd}_{0.75}\text{S}$	CdS
Excitonic emission						
Defect activated emission (eV)	E1 (V_S-V_B)	2.56	2.42	2.21	2.02	2.03
	E2 (V_S-I_S)	2.42 <i>green</i>	2.24 <i>green</i>	2.07 <i>yellow</i>	1.91 <i>red</i>	1.90 <i>red</i>
	E3 (V_S-V_M)	2.27	2.07	1.89	1.71	1.71

Italicized values indicate the maximum PL intensity and visible emission color

The diffraction peaks observed in the XRD pattern of ZnS QDs (Fig. 3a) at 2θ at $28.6 \pm 0.1^\circ$, $47.8 \pm 0.1^\circ$, and $56.5 \pm 0.1^\circ$ can be assigned to the planes (111), (220), and (311) of ZnS cubic lattice structure (Zinc blend also referred to as sphalerite, JCPDS 05-0566). Analogously, the peaks at 2θ values of $26.6 \pm 0.1^\circ$, $43.9 \pm 0.1^\circ$, and $52.2 \pm 0.1^\circ$ (Fig. 3c) can be indexed to the planes (111), (220), and (311) of the cubic structure CdS (ICCD 89-0440), respectively. The $\text{Zn}_{0.50}\text{Cd}_{0.50}\text{S}$ sample (Fig. 3b) also has a cubic crystal phase with diffraction peaks shifted relative to the two binary systems and located at an intermediary value between ZnS and CdS. As the ionic radius of Zn^{2+} is smaller than that of Cd^{2+} , the addition of Cd atoms to ZnS structure caused diffraction peaks to shift to lower angles with a correspondent increase of the unit-cell volume of the $\text{Zn}_{0.50}\text{Cd}_{0.50}\text{S}$ sample in comparison with ZnS. Thus, it evidenced that a homogeneous alloyed solid solution has been achieved by controlling the stoichiometric ratio of Zn:Cd. In addition, the broad band present at $2\theta \sim 21.8^\circ$ (Fig. 3d) is characteristic of the CMCEl polymer used for the chemical stabilization of the metal sulfide QDs [38].

In order to access the morphological features and the sizes of the $\text{Zn}_x\text{Cd}_{1-x}\text{S}$ systems ($x = 1.0, 0.50$, and 0), TEM analysis was performed and the typical images are showed in Fig. 4A (ZnS), Fig. 4B ($\text{Cd}_{0.50}\text{Zn}_{0.50}\text{S}$), and Fig. 4C (CdS). TEM images confirm the formation of QDs with reasonable spherical shape and similar sizes (average diameter \pm standard deviation) of 4.9 ± 0.5 nm for CdS, 4.3 ± 0.3 nm for ZnS, and 4.3 ± 0.5 nm for $\text{Zn}_{0.50}\text{Cd}_{0.50}\text{S}$. The clear two-dimensional crystal lattice stripes obtained by selected area electron diffraction (SAED patterns) in the TEM images demonstrate the crystalline nature of the QDs and indicate the formation of nanocrystals with cubic structure and lattice parameters consistent with the 2θ diffraction angles obtained by XRD.

From the materials science perspective, the properties of the semiconductor nanoalloys produced were interpreted considering empirical and semi-empirical models. Therefore, Vegard's law empirical rule widely used in metallurgy to predict the physical and optical properties of materials was used to validate the relationship that the lattice constant and bandgap energy would be changed depending on the concentration of

**Fig. 3** X-Ray diffraction analysis of conjugates. XRD patterns of ZnS (a), $\text{Zn}_{0.50}\text{Cd}_{0.50}\text{S}$ (b), CdS (c), and CMCEl ligand (d)

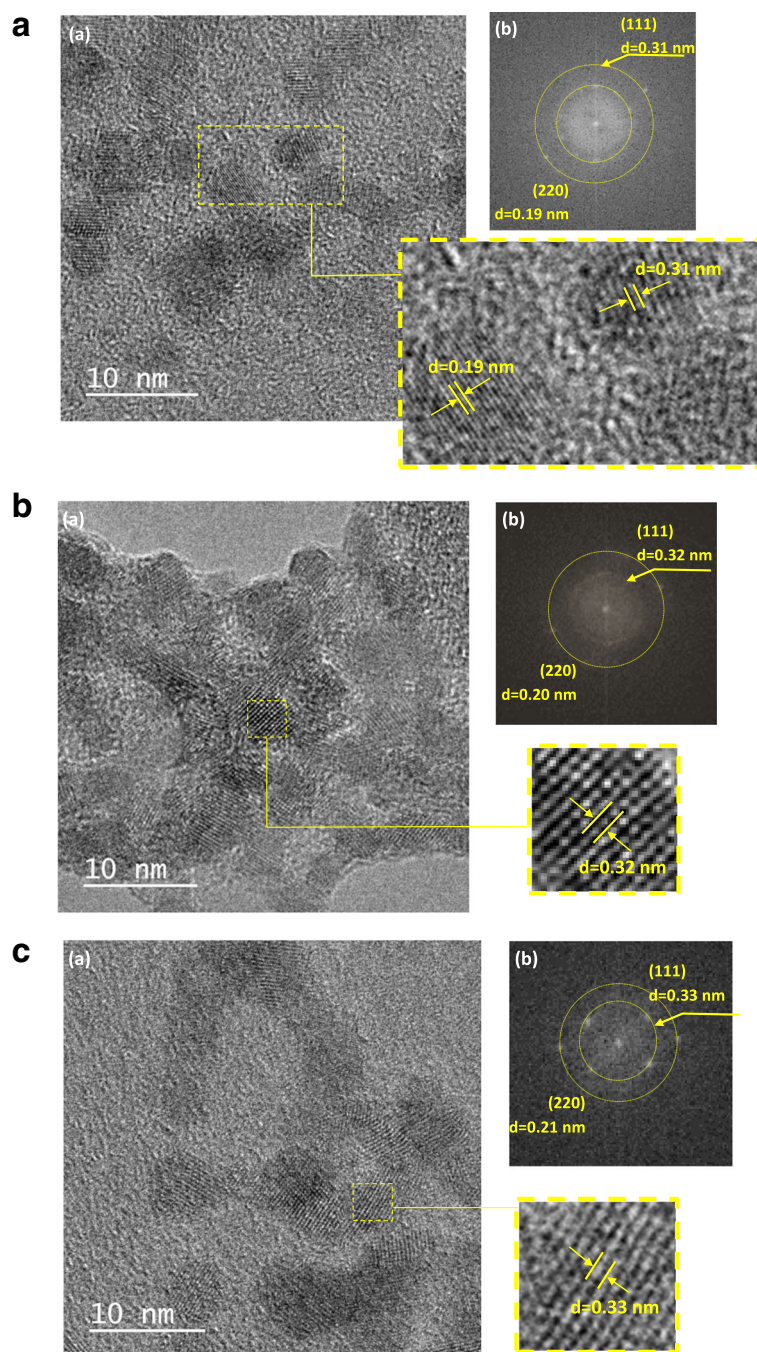


Fig. 4 Transmission electron microscopy characterization of conjugates; (a) TEM image with SAED patterns (detail) and (b) diffraction rings attributed to (111) and (220) planes of the cubic lattice (d = interplanar distance) for **a** ZnS, **b** $\text{Zn}_{0.50}\text{Cd}_{0.50}\text{S}$, and **c** CdS QDs

the constituents [18, 39, 40]. Therefore, by the combination of wide-bandgap (ZnS, $E_g = 3.61$ eV) with medium-bandgap (CdS, $E_g = 2.42$ eV) semiconductors [28], it was predicted a linear reduction of the energy of absorption of the alloyed metal sulfide system as the concentration of Cd^{2+} was increased, following the Vegard's law, Eq. 3.

$$E_g^{\text{alloy}}(\text{Zn}_x\text{Cd}_{1-x}\text{S}) = x E_g(\text{ZnS}) + (1-x) E_g(\text{CdS}), \quad 1.0 > x > 0 \quad (3)$$

However, it can be observed in Fig. 5a that the experimental results of bandgap energies and PL emission of the $\text{Zn}_x\text{Cd}_{1-x}\text{S}$ ternary nanoalloys presented a deviation

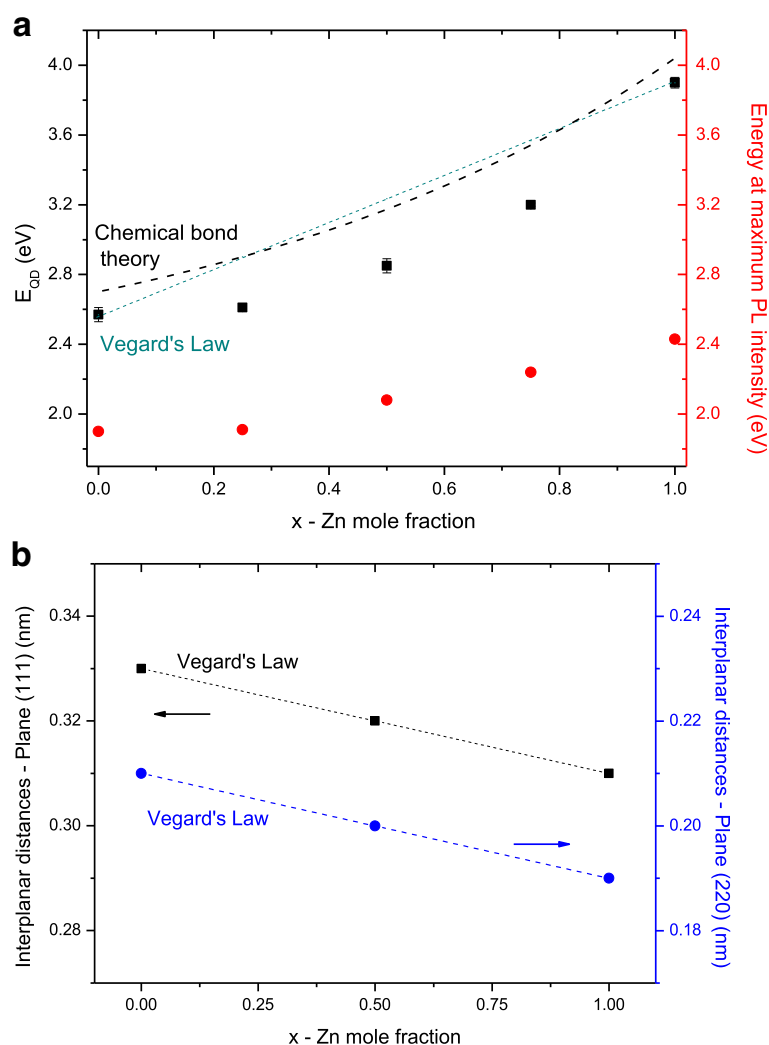


Fig. 5 Empirical and semi-empirical models of semiconductor nanoalloys. **a** Non-linear relationship of E_{QD} (squares) and PL wavelength (circles) as a function of the molar content of Zn^{2+} . Dotted line indicates Vegard's law (calculated) and dashed line, the expected values based on Chemical Bond Theory (from reference [45]). **b** Linear relationship of lattice parameters as a function of the concentration of Zn^{2+} in the material (data from ED analysis)

to lower values as a general trend from the Vegard's law plot (dotted line), except for pure QDs (i.e., ZnS or CdS), which were used as reference for constructing this equation. Both optical properties, absorption and emission, were significantly affected by the composition of the $Zn_xCd_{1-x}S$ alloys but with distinct energies from the predicted linear behavior of Vegard's law. In general, similar to Vegard's law [39], other models are used for calculating the correlation of optical properties with the size and composition of semiconductor nanocrystals, such as effective mass approximation (EMA) [41], semi-empirical tight-binding model (TBM) [42], and chemical bond model (CBM) [43–45]. Nonetheless, they usually overestimate the bandgap energies under the quantum confinement of the exciton mainly because of simplified assumptions such as by considering a spherical volume

of the nanocrystallite, minimizing the complexity and reducing the parameters involved [42, 44]. Although not accurate and valid for all ternary and quaternary alloyed QDs, the chemical bond model (CBM) [43–45], which is not a linear function, is suggested as more adequate for correlating the effect of quantum dependence of optical properties (bandgap energy) with the concentration of alloyed QDs such as $Zn_xCd_{1-x}S$ (dashed line). It can be noted that the CBM plot from the literature [45] with the similar system but with different surface ligand and alloy compositions ($Zn_xCd_{1-x}S$, $x = 0$ to 0.42, and QD size of 4.4 nm) presented overestimated values of approximately ~200 meV compared to our experimental data. However, the shape of the curve resemble more similarly than linear Vegard's law, due to the combination of parameters related to quantum confinement (inner

QD) and chemical interactions with ligands at the surface (outermost layer of QD) in the CBM model [44, 45].

It is worth mentioning that the red shift of the emission with respect to absorption spectra (known as Stokes shift) increased with raising the Zn^{2+} concentration in the $\text{Zn}_x\text{Cd}_{1-x}\text{S}$, from $x = 0$ to 1.0 (Fig. 5a) due to the complex mechanism of separation and recombination of charges in the nanoalloys. Essentially, based on Brus' equation [41], who developed the first theoretical calculation for semiconductor nanoparticles named EMA model (Eq. 4), an exciton is considered to be confined to a spherical volume of the nanocrystallite and the mass of electron and hole is replaced with effective masses (m_e and m_h) to define the wave function. Hence, the higher reduced mass of exciton (Eq. 5, $1/\mu$) of ZnS ($m_e^* = 0.25$, $m_h^* = 0.59$) compared to CdS ($m_e^* = 0.21$, $m_h^* = 0.80$) increased its relative blue shift by approximately 6% (ΔE_g , Eq. 6, where h is the Planck's constant) associated with the quantum confinement, which was indeed verified by increasing the concentration of Zn^{2+} in the alloyed QDs of $\text{Zn}_x\text{Cd}_{1-x}\text{S}$.

$$E_{\text{QD}} = E_g + \Delta E_g \quad (4)$$

$$1/\mu = 1/m_e^* + 1/m_h^* \quad (5)$$

$$\Delta E_g \approx h^2/8\mu R^2 \quad (6)$$

Nonetheless, a distinct behavior was observed for the physical properties (e.g., interplanar distances), where a linear correlation was observed by varying the ternary alloy composition in agreement with the literature [20]. Figure 5b shows the lattice spacing for (111) and (220) planes calculated from ED patterns (TEM images). The interplanar distances exhibit a linear behavior upon changing the x values according to Vegard's law evidencing that the $\text{Zn}_{0.50}\text{Cd}_{0.50}\text{S}$ system is an alloyed QD instead of a mixture of CdS and ZnS nanocrystals.

To perform a more in-depth characterization of $\text{Zn}_{0.50}\text{Cd}_{0.50}\text{S}$ QDs at nanoscale order, EFTEM coupled with EELS and XPS measurements were performed. Energy-filtered transmission electron microscopy (EFTEM) with low-loss electron energy-loss spectroscopy (EELS) yields new possibilities for the investigation of alloyed ternary nanomaterials [46, 47]. Therefore, the elemental distribution of $\text{Zn}_{0.50}\text{Cd}_{0.50}\text{S}$ QDs was assessed using EELS/EFTEM techniques to investigate the distribution of Cd and Zn in the synthesized $\text{Zn}_{0.50}\text{Cd}_{0.50}\text{S}$ QDs, which was selected as a typical alloyed ternary system. Figure 6a shows a zero energy loss image of an isolated QD, and Fig. 6b, c shows the chemical composition maps of Cd and Zn at nanometer resolution. The uniform distribution of the Zn and Cd elements demonstrated the formation of homogeneous alloyed $\text{Zn}_{0.50}\text{Cd}_{0.50}\text{S}$ QDs, supporting the XRD and TEM results. Moreover, the thermodynamics and kinetics

favor the formation of homogenous alloyed ternary QDs as the Gibbs free energy of formation of ZnS and CdS are of the same magnitude ($\sim 180\text{--}200 \text{ kJ mol}^{-1}$) and the solubility product constant are very low ($k_{\text{sp}} \sim 10^{-25}\text{--}10^{-27}$) in the presence of excess of sulfides in the reaction medium at room temperature.

Figure 7a–e shows typical XPS spectra obtained directly at the surface of the conjugate composed of $\text{Zn}_{0.50}\text{Cd}_{0.50}\text{S}$ -CMC. Figures 7a, b shows representative spectra of C 1s and O 1s regions, respectively. Both spectra are showed several peaks that were identified by deconvolution procedure [48]. C 1s spectrum revealed different chemical bonds of carbon atoms: C–H and C–C bonds at binding energy of 284.5 eV; C–O bond at 286.2 eV; one peak at 287.9 eV assigned to C=O and O–C–O bonds; and O=C–OR bonds at 290.6 eV [48, 49]. Peaks of O=C and O–C at 531.7 and 532.9 eV, respectively, were observed in the O 1s region [49]. These XPS spectra are compatible with the chemical structure of CMC. In addition, XPS spectra at the surface of the quantum dot–CMC conjugates in the regions related to Zn 2p (Fig. 7c), Cd 3d (Fig. 7d), and S 2p (Fig. 7e) indicated no detectable signal from zinc, cadmium, and sulfur, respectively. This result demonstrated the presence of an organic shell of CMC used as capping agent of QD nanoparticles for controlling the nucleation and limiting the growth of the alloyed nanocrystals just formed in the colloidal media within the quantum confinement regime. Due to the expected repulsion between negatively charged CMC chains associated with carboxylate groups, this organic shell is probably composed of a monolayer surrounding the semiconductor core, which is complex to be precisely measured [50]. Thus, in order to get the distribution of the elements at the surface underneath this CMC layer, ion bombardment with argon ions (Ar^+ , 1 cycle, 10 s, emission current 10 mA, and beam voltage 0.5 kV) was applied for removing the organic shell. The corresponding elemental composition of the QD surface obtained by XPS spectroscopy taken for Zn 2p, Cd 3d, and S 2p regions is showed in Fig. 7f–h. First, it can be observed that the three chemical elements of the ternary systems were detected, in agreement with the previous results that indicated the formation of ternary nanoalloy. In Fig. 7f, the peaks at 1021.8 and 1044.8 eV correspond to the $\text{Zn } 2p_{3/2}$ and $\text{Zn } 2p_{1/2}$ levels, respectively, and are associated with the Zn (2p) transitions in ZnS. The spin-orbit components ($\text{Zn } 2p_{3/2}$ and $\text{Zn } 2p_{1/2}$) are separated by a binding energy interval of approximately 23.0 eV [49, 51–53]. The two strong peaks in Fig. 7g at 411.7 eV ($\text{Cd } 3d_{3/2}$) and 404.9 eV ($\text{Cd } 3d_{5/2}$) are generally assigned to Cd–S bonding in CdS. The difference between the binding energies of $\text{Cd } 3d_{5/2}$ and $\text{Cd } 3d_{3/2}$ is 6.8 eV, in agreement with the literature [30, 49, 53]. The S $2p_{3/2}$ peak (Fig. 7h)

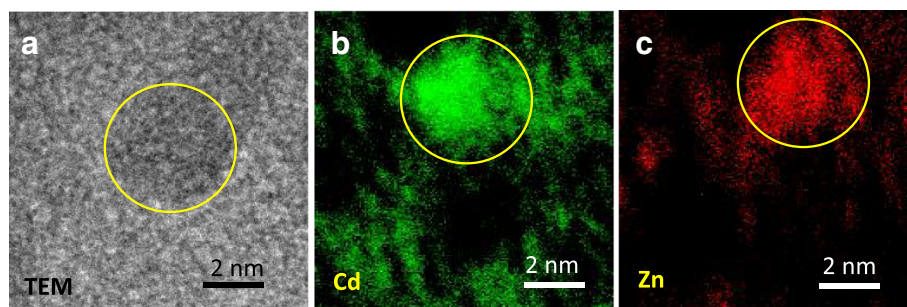


Fig. 6 EELS and EFTEM analyses of conjugates. EFTEM Elemental maps of Cd and Zn in samples of $\text{Zn}_{0.50}\text{Cd}_{0.50}\text{S}$ quantum dots. **a** EFTEM zero energy loss image of an individual $\text{Zn}_{0.50}\text{Cd}_{0.50}\text{S}$ quantum dot. **b** EELS signals of Cd forming the composition map (Cd M edge at 404 eV). **c** EELS signals of Zn forming the composition map (Zn L edge at 1020 eV)

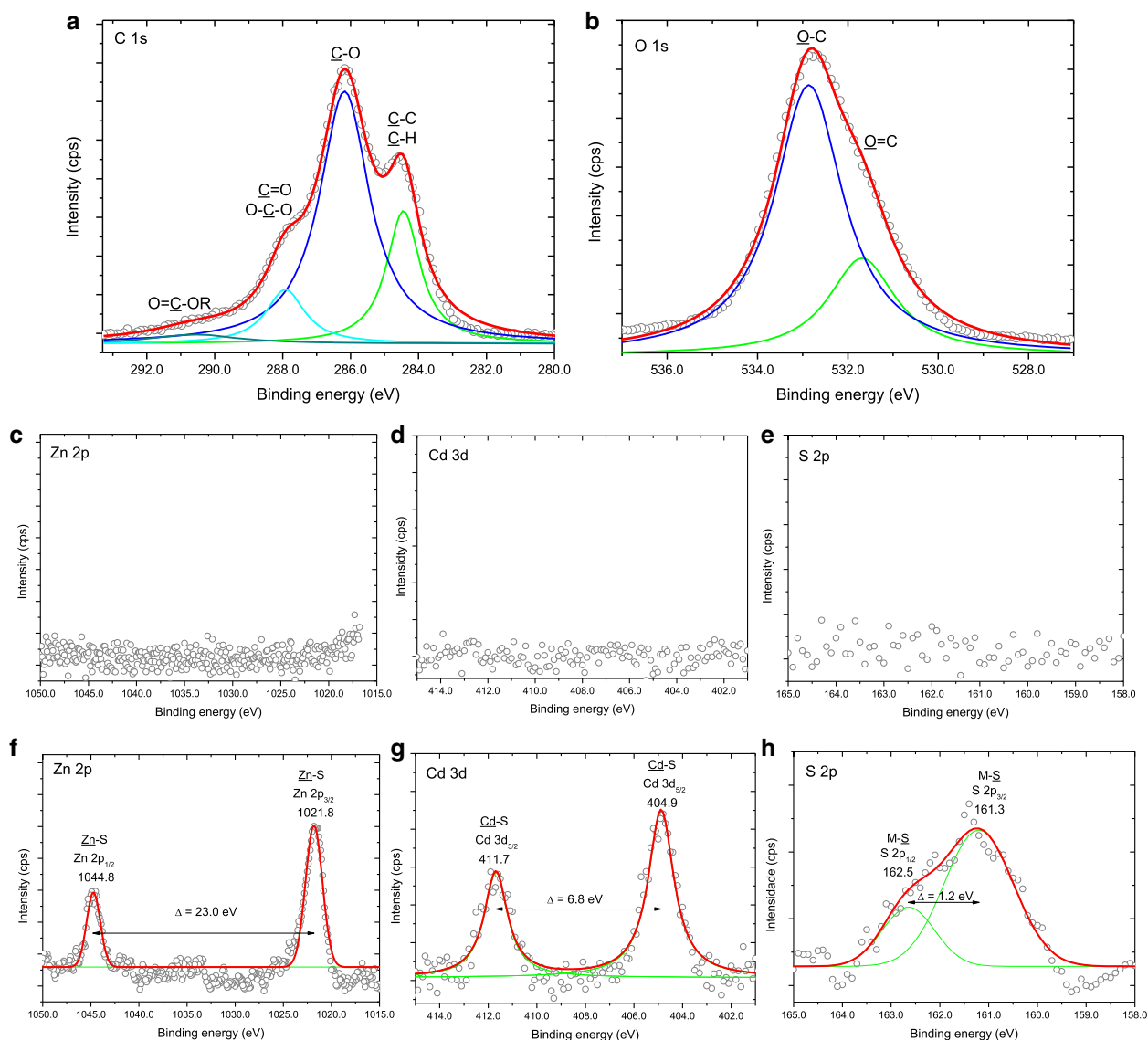


Fig. 7 X-ray photoelectron spectroscopy of conjugates. XPS spectra of C 1s (**a**), O 1s (**b**), Zn 2p (**c**), Cd 3d (**d**), and S 2p (**e**) regions at the surface of $\text{Zn}_{0.50}\text{Cd}_{0.50}\text{S}$ ternary system and XPS spectra of Zn 2p (**f**), Cd 3d (**g**), and S 2p (**h**) regions after etching

and S $2p_{1/2}$ peaks were found at 161.3 and 162.5 eV, respectively, ($\Delta = 1.2$ eV), which can be assigned to sulfur in metal sulfides (M–S) [49, 51–53]. Elemental analysis data was determined from the integrated area of Cd 3d, Zn 2p, and S 2p signals with appropriate atomic sensitivity factors using the XPS software for data processing (Vision Processing, Kratos).

Despite neglecting effects of spherical particle geometry, small QD size, and preferential sputtering, the outmost surface of the QDs presented atomic concentrations (%) of Zn, Cd, and S of $50 \pm 4\%$, $16 \pm 2\%$, and $33 \pm 3\%$, respectively. As expected, distinct from the homogenous composition of the “inner” portion of the nanocrystals, the XPS results of the surface indicated depletion in sulfur content and, therefore, a metal enriched surface (with $[Zn^{2+}] > [Cd^{2+}]$). This metal-rich outmost layer can be assigned to the formation of complexes at the surface involving the cations (i.e., Cd^{2+} and Zn^{2+}) and groups of the polymer capping ligands [54–57] that compete with sulfide (S^{2-}) ions. The relatively higher concentration of Zn^{2+} compared to Cd^{2+} at the QD surface is attributed to the hardness parameter derived from electronegativity, where Zn(II) forms more stable complexes with both oxygen and nitrogen than Cd(II). The stability of complexes of divalent ions in the transition metal series with chelators containing oxygen or nitrogen donors often follows the Irving–Williams order [58, 59]. Conversely, the concentration of sulfides at the surface of QDs is decreased by the repulsion of the anionic carboxylate groups of the CMCell polymer ligand. In addition, this ZnS-rich outermost layer may act as an encapsulating coating of wider bandgap over the homogeneous nanocrystalline “core” that physically separates the surface of the optically active core and reduces the number of dangling bonds that can act as non-radiative surface states that quench PL intensity [60, 61]. Hence, the XPS results evidenced that QD conjugates were produced with core-shell nanostructure composed of alloyed ternary $Zn_xCd_{1-x}S$ inorganic core and carboxymethylcellulose organic shell uniformly dispersed and stabilized in aqueous media as depicted in Fig. 8.

Zeta potential (ζ) measurements evidenced the interactions of QDs with carboxylate groups at the nanoparticle–polymer interfaces and the role of these groups in the stabilization of the QDs. The measured ζ -potentials were all negative values, -52 ± 5 mV (ZnS), -53 ± 6 mV (ZnCdS), and -56 ± 8 mV (CdS), lower than -72 mV of CMCell solution, probably because of metal complexes remained at the nanocrystal–polymer interface (QD–CMCell). In addition, these highly negative values (i.e., $\zeta \leq -50$ mV) indicated that the nanoparticles were electrostatically stabilized by CMCell carboxylate functional groups avoiding the growth and agglomeration of the nanocrystals, which is crucial for quantum-size confinement effects. Moreover, the morphological and stability

features of these colloidal ZnCdS conjugates in aqueous medium were assessed by DLS analysis. Thus, the DLS results showed that the systems were produced with hydrodynamic diameters (H_D) of 12.5 ± 1.3 nm, 11.8 ± 0.8 nm, and 8.0 ± 0.5 nm for ZnS, ZnCdS, and CdS, respectively. The H_D is assigned to the sum of contributions from the inorganic QDs “core” and the CMCell organic “shell” of the conjugates, including the effect of solvation layers and the lateral extension of the capping ligands. The DLS measurements clearly indicated a lower volume of solvation for the CdS that may be associated with the type, extension, and/or stability of the Cd^{2+} chelate complex with chemical groups of the carboxymethylcellulose compared to Zn^{2+} , which probably caused the higher contraction of the polymeric shell around the Cd-based QD inorganic core.

Biological Characterization of $Zn_xCd_{1-x}S$ QD Conjugates

Evaluation of Cytotoxicity by MTT Cell Viability Assay

MTT (3-[4,5-dimethylthiazol-2-yl]-2,5-diphenyltetrazolium bromide) assay accesses the mitochondrial activity response of cells, which is suitable for evaluating the cell viability and cytotoxicity towards the QD conjugates. The results of MTT assay after 120 h of contact of the cells with ZnS, $Zn_{0.50}Cd_{0.50}S$, and CdS conjugates at concentration of 10 nM are presented in Fig. 9A. It demonstrated that, within the statistical variation, no difference was found in the cell viability after 5 days of incubation with the ZnS and $Zn_{0.50}Cd_{0.50}S$ conjugates when compared to the control condition validating the hypothesis of non-toxicity associated with ZnS and alloyed $Zn_{0.50}Cd_{0.50}S$ conjugates. Conversely, for CdS samples, as previously reported in the literature [62, 63], an adverse reduction of approximately 30% of cell viability response ($\sim 70\%$ viability) was verified, which was attributed predominately to the potential cytotoxicity caused by release of Cd^{2+} . Therefore, it was demonstrated that the CMCell polymer played multiple functions for chemically stabilizing and rendering biocompatible ZnS and $Zn_{0.50}Cd_{0.50}S$ conjugates. Moreover, the Zn-rich outmost surface of $Zn_{0.50}Cd_{0.50}S$ conjugates, besides enhancing the optical properties compared to pure binary QDs (i.e., ZnS and CdS) as discussed in previous section, it may have also played a relevant role for improving the biocompatibility by hindering the contact of the Cd-alloyed core with the water medium and, therefore, impeding the release of Cd^{2+} .

Cellular Uptake of $Zn_xCd_{1-x}S$ QD Conjugates by Laser Scanning Confocal Microscopy

In the present study, as a proof of concept, the uptake process of $Zn_{0.50}Cd_{0.50}S$ and ZnS QD conjugates by live cells was performed by laser scanning confocal microscopy. CdS conjugates were not tested as it has already proved to reduce cell viability by the MTT assay results discussed in the previous section. On the other hand, ZnS QDs have

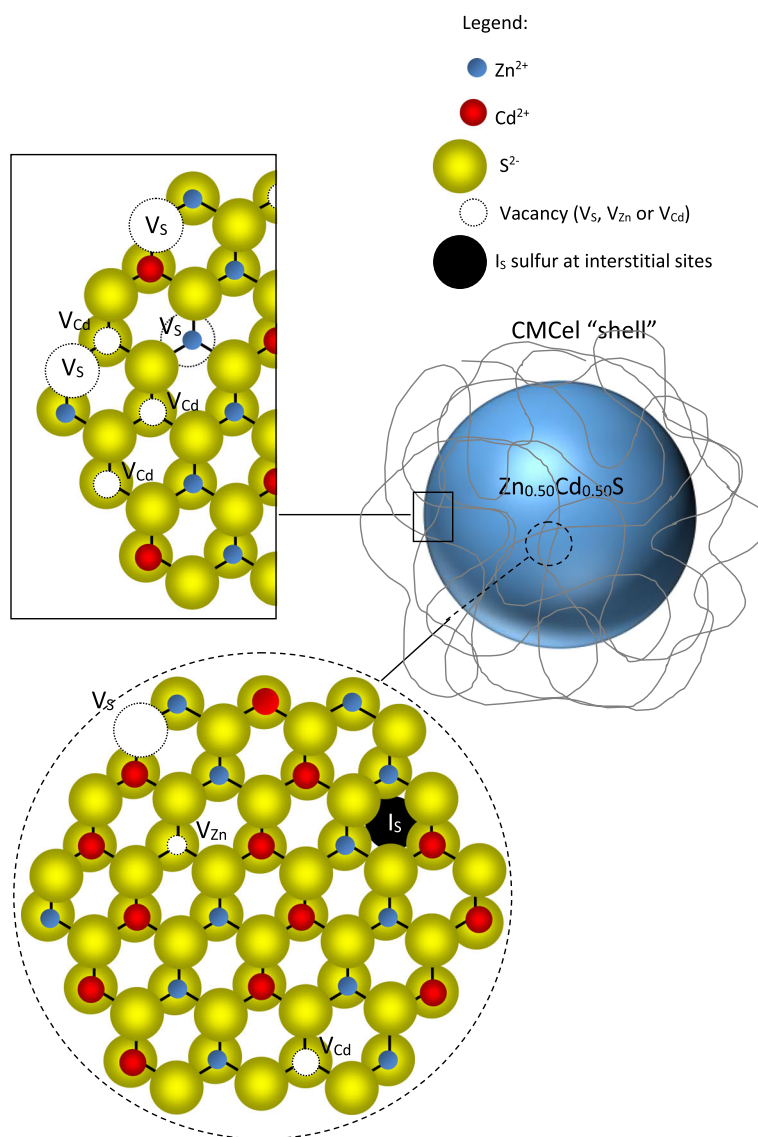


Fig. 8 Drawing of $\text{Zn}_{0.50}\text{Cd}_{0.50}\text{S}$ quantum dot stabilized by CMC polymer; Schematic representation of $\text{Zn}_{0.50}\text{Cd}_{0.50}\text{S}$ quantum dot (not to scale)

been reported to be safe and non-toxic for in vitro endocytosis and cellular imaging assays. Thus, for the cellular internalization assay, HEK293T cells were incubated for 1 h with $\text{Zn}_{0.50}\text{Cd}_{0.50}\text{S}$ and ZnS conjugates at final concentration of 500 nM. After this period of incubation, images were captured using laser confocal microscopy for the purpose of visualizing the internalization of the developed surface-biofunctionalized ZnS and $\text{Zn}_{0.50}\text{Cd}_{0.50}\text{S}$ QDs. Figure 9B shows that the $\text{Zn}_{0.50}\text{Cd}_{0.50}\text{S}$ (A) and ZnS (B) conjugates were effectively internalized by HEK293T cells. Based on these confocal microscopy images, it was verified that $\text{Zn}_{0.50}\text{Cd}_{0.50}\text{S}$ and ZnS conjugates were cytocompatible as they penetrated through the cell membrane and were found homogeneously distributed inside the cellular cytoplasm. Therefore, these findings combined with MTT

results highlight the suitability of using ZnS and alloyed $\text{Zn}_{0.50}\text{Cd}_{0.50}\text{S}$ QDs capped by CMCel ligand as fluorescent nanoprobes for in vitro cellular imaging and labeling applications. Although it is a fascinating area of research, a more in-depth investigation is beyond the scope of this work and will certainly be subject of future studies.

Photocatalytic Activity of $\text{Zn}_x\text{Cd}_{1-x}\text{S}$ QD Conjugates for environmental Applications

Photocatalysis is a rapidly expanding technology for wastewater treatment. For that reason, using a multifunctional approach, here it is presented as a proof of concept, preliminary tests using the ZnS and alloyed $\text{Zn}_{0.50}\text{Cd}_{0.50}\text{S}$ conjugates as nano-photocatalysts for the degradation of methylene blue (MB) used as a model

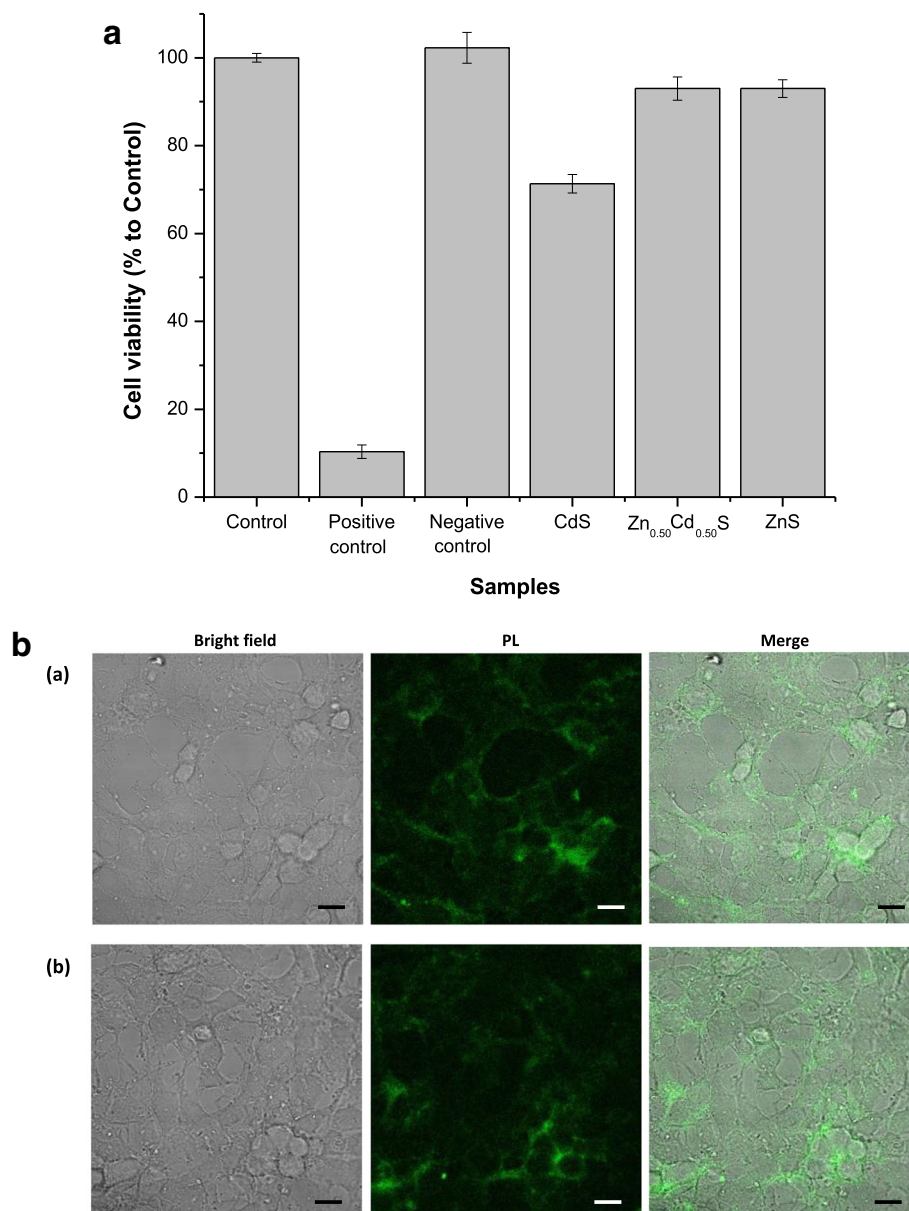


Fig. 9 MTT cell viability in vitro assay of conjugates. **a** MTT cell viability assay of HEK293T cells after 120 h of contact of cells with ZnS, Zn_{0.50}Cd_{0.50}S, and CdS conjugates. **b** Confocal microscopy imaging of the internalization of the (a) Zn_{0.50}Cd_{0.50}S and (b) ZnS conjugates in the HEK293T cells (scale bar = 10 μ m)

organic dye pollutant under UV irradiation. The results of degradation efficiency and UV-vis spectra after 4 h of irradiation are summarized in Fig. 10A, B, respectively. Based on Eq. 2, it was found that ZnS conjugates bleached MB relatively faster (first-order rate constant $k = 0.37 \text{ h}^{-1}$) than Zn_{0.50}Cd_{0.50}S sample ($k = 0.27 \text{ h}^{-1}$) within the first 2 h but with similar degradation efficiency ($58\% \pm 2\%$) after 4 h of photocatalytic test (Fig. 10A). As both conjugates presented equivalent QD sizes (i.e., 4.3 nm) and surface areas, the minor difference observed for the catalysis kinetics rate can be

associated with the presence of a Zn-rich outmost surface layer in the alloyed QD (Zn_{0.50}Cd_{0.50}S). It is suggested that the wider bandgap surface layer of ZnS over the narrower bandgap Zn_{0.50}Cd_{0.50}S nanocrystal decreased the density of surface defects (i.e., energy trap states) promoting faster excitonic recombination process inside the semiconductor core. Therefore, this diminution of charge carrier separation (i.e., electron-hole pairs) caused the reduction of generated reactive species crucial for the photocatalytic activity to degrade MB molecules.

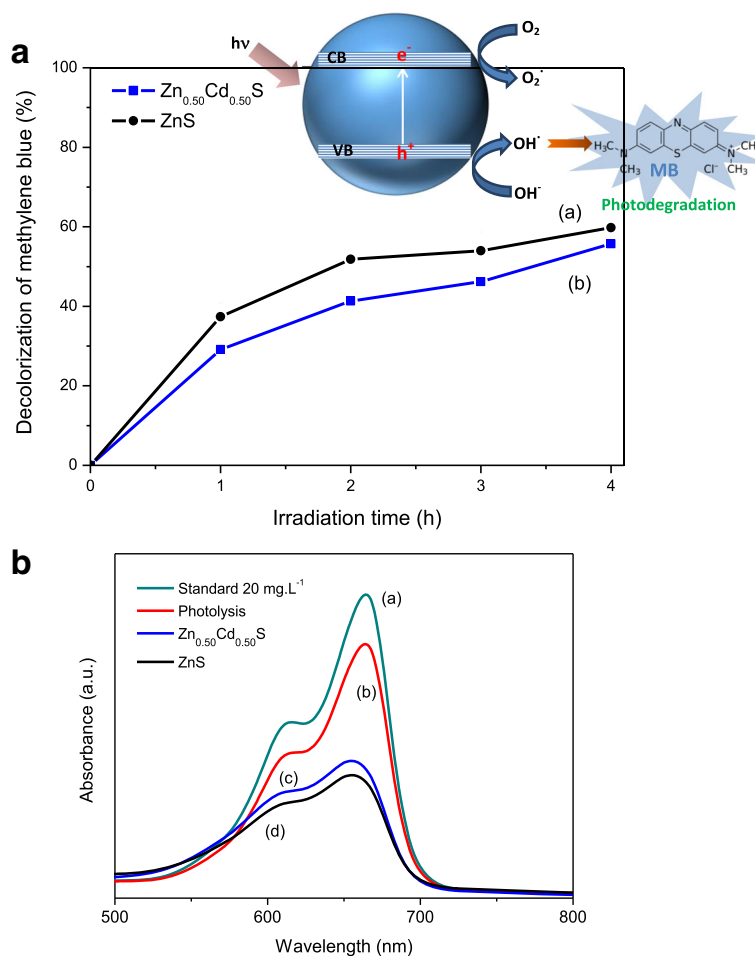


Fig. 10 Photocatalysis application of conjugates. **a** Decolorization of methylene blue (MB) in aqueous solution by nanophotocatalyst ZnS (a) and $\text{Zn}_{0.50}\text{Cd}_{0.50}\text{S}$ (b). *Inset drawing*: schematic organic dye degradation by conjugates. **b** Absorption spectra of MB aqueous solution: reference solution (a) and degraded by light (control) (b), $\text{Zn}_{0.50}\text{Cd}_{0.50}\text{S}$ (c) and ZnS (d) conjugates under UV light after 4 h

Analogously, it can be observed the reduction of absorbance associated with the color of MB at $\lambda = 664$ nm (Fig. 10B) caused by the photo-oxidation of the MB molecule, shifting the absorption peaks to lower wavelength (blue shift). This photodegradation is related to chemical species generated by electron-hole pairs ($\text{QD} + h\nu \rightarrow h^+ / e^-$) from irradiated QDs (i.e., ZnS or $\text{Zn}_{0.50}\text{Cd}_{0.50}\text{S}$, Fig. 10A, inset drawing). The oxidation mechanism is primarily governed by the valence band holes (h^+), which are powerful oxidants, and they can react with water or surface-bound chemisorbed hydroxyl groups (OH^-) producing hydroxyl radicals (OH^\bullet). Most organic photodegradation reactions utilize the strong oxidizing power of the holes directly or indirectly produced by excitation of nanomaterials [64–66]. It is reasonable to consider that this degradation of MB may have followed a double-stage process. Initially, the negatively charged CMCell polymer is likely to have attracted MB molecules (i.e., positively charged) leading to the adsorption process,

which does not degrade or promote decolorization of MB. In the sequence, the photo-oxidation of the MB dye occurred by the photocatalytic process, which was enhanced by previous adsorption favoring the charge exchange at the conjugate-MB interfaces (i.e., h^+ / e^- scavenging).

Regarding to toxicity, some researchers have raised concerns about the environmental safety related to the use of nanomaterials composed with toxic elements such as Cd-containing QDs motivated by the possibility of photo-oxidation with eventual releasing of hazardous elements in the medium [67, 68]. However, despite the hypothetical possibility, it is not likely to occur in these alloyed conjugates because of the biocompatible organic shell encapsulating the inorganic core, the extremely low concentration of the metallic elements (i.e., from μM to nM), associated with the very low water solubility of their compounds (e.g., oxides, sulfates, hydroxides) minimizing eventual risk of contamination.

Thus, these results demonstrated that ZnS and $\text{Zn}_x\text{Cd}_{1-x}\text{S}$ semiconductor conjugates were surface functionalized by carboxymethylcellulose using a novel green sustainable process, which can offer promising alternatives as nano-platforms in environmental and biomedical applications.

Conclusions

In this study, it is presented the synthesis and characterization of new ternary alloyed $\text{Zn}_x\text{Cd}_{1-x}\text{S}$ semiconductor QDs using carboxymethylcellulose as a biocompatible polymer capping ligand directly produced via eco-friendly colloidal process in aqueous media and at room temperature. XPS results evidenced the mechanism of stabilization of the $\text{Zn}_x\text{Cd}_{1-x}\text{S}$ nanoalloys dominated by the chemical interactions of metal-rich surface ($\text{Zn}^{2+} > \text{Cd}^{2+} > \text{S}^{2-}$) with the carboxylates and hydroxyls groups of the polymer ligands. The EELS, TEM, XRD, and selected area electron diffraction analyses ruled out the formation of core-shell or multiphase systems, demonstrating that homogenous $\text{Zn}_x\text{Cd}_{1-x}\text{S}$ nanoalloys were produced with optical absorption and emission dependent on the concentration of Zn^{2+} . In addition, it was observed that the composition of ternary $\text{Zn}_{0.5}\text{Cd}_{0.5}\text{S}$ alloys improved the luminescence quantum yield compared to the pure binary systems (ZnS and CdS QDs). These optical properties of $\text{Zn}_x\text{Cd}_{1-x}\text{S}$ nanoalloys were studied based on empirical model of Vegard's law and chemical bond model (CBM), where the differences observed of the values were assigned to the bandgap structure of each system. Moreover, in order to provide insights about potential applications of these alloyed-QD conjugates, they were tested for live cell imaging and for photocatalysis of organic molecules. The results demonstrated that ZnS and $\text{Zn}_{0.5}\text{Cd}_{0.5}\text{S}$ conjugates were non-toxic and behaved as effective fluorophores for in vitro imaging live human embryonic kidney cells (HEK293T) with confocal fluorescence microscopy. Additionally, these alloyed-QD conjugates presented photocatalytic activity for photodegradation of methylene blue, which was used as model organic industrial pollutant in water. Hence, composition-tunable optical properties of ternary $\text{Zn}_x\text{Cd}_{1-x}\text{S}$ ($x = 0\text{--}1.0$) fluorescent alloyed QDs was verified based on a facile eco-friendly process. It is foreseen that this class of alloyed fluorescent semiconductor nanocrystals offers several possibilities of bandgap engineering for multiple applications such as biolabeling and bioimaging in nanomedicine or as nano-photocatalyst for environmental purposes in water treatment.

Acknowledgements

The authors acknowledge the financial support from the following Brazilian research agencies: CAPES—Coordenação de Aperfeiçoamento de Pessoal de Nível Superior (PROEX-433/2010;PNPD;PROINFRA2010-2014), FAPEMIG—Fundação de Amparo à Pesquisa do Estado de Minas Gerais (PPM-00202-13;BCN-TEC 30030/12), CNPq—Conselho Nacional de Pesquisa (PQ1B-306306/2014-0; UNIVERSAL-457537/2014-0), and FINEP—Financiadora de Estudos e Projetos (CTINFRA-PROINFRA 2008/2010/2011). The authors express their gratitude to the staff at the

Microscopy Center at UFMG for their assistance with TEM-EFTEM-EELS analysis and Prof. A. Bicalho for XRD experiments. The authors thank the staff at the Center of Nanoscience, Nanotechnology and Innovation-CeNano²/CEMUCAS/UFMG for the spectroscopy analyses. Finally, the authors thank Universidade Federal de Minas Gerais—UFMG/PRPq for the financial support for the publication of this study (PRPq—02/2017).

Authors' contributions

HSM carried out the experimental design and analysis and drafted the manuscript. AAPM carried out the synthesis, physicochemical characterization, and analysis of conjugates and drafted the manuscript. RLM carried out the synthesis, physicochemical characterization, and analysis of conjugates. AJC designed, performed, and analyzed TEM, SAED, EFTEM-EELS experiments. LCO designed, performed, and analyzed the photocatalysis experiments. All authors read and approved the final manuscript.

Competing interests

The authors declare that they have no competing interests.

Publisher's Note

Springer Nature remains neutral with regard to jurisdictional claims in published maps and institutional affiliations.

Author details

¹Center of Nanoscience, Nanotechnology and Innovation - CeNano(2), Department of Metallurgical and Materials Engineering, Universidade Federal de Minas Gerais—UFMG, Belo Horizonte, Brazil. ²Department of Chemistry, Universidade Federal de Minas Gerais—UFMG, Belo Horizonte, Brazil. ³Federal University of Minas Gerais, Av. Antônio Carlos, 6627 - Escola de Engenharia, Bloco 2 - Sala 2233, Belo Horizonte, MG 31.270-901, Brazil.

Received: 4 May 2017 Accepted: 25 June 2017

Published online: 05 July 2017

References

- Farber E (1960) A history of metals. *Science* 132:887–888
- An L, Yu Y, Li X, Liu W, Yang H, Wu D, Yang S (2014) Dextran-coated superparamagnetic amorphous Fe–Co nanoalloy for magnetic resonance imaging applications. *Mater Res Bull* 49:285–290
- Farle M (2017) Imaging techniques: nanoparticle atoms pinpointed. *Nature* 542:35–36
- Ferrando R, Jellinek J, Johnston RL (2008) Nanoalloys: from theory to applications of alloy clusters and nanoparticles. *Chem Rev* 108:845–910
- Qin Z, Zhang F (2013) Surface decorated $\text{Cd}_x\text{Zn}_{1-x}\text{S}$ cluster with CdS quantum dot as sensitizer for highly photocatalytic efficiency. *Appl Surf Sci* 285P:912–917
- Ayelele DW, Suc W, Chou H, Pan C, Hwang B (2014) Composition-controlled optical properties of colloidal CdSe quantum dots. *Appl Surf Sci* 322:177–184
- Shen S, Wang Q (2013) Rational tuning the optical properties of metal sulfide nanocrystals and their applications. *Chem Mater* 25:1166–1178
- Zhou J, Yang Y, Zhang C-Y (2015) Toward biocompatible semiconductor quantum dots: from biosynthesis and bioconjugation to biomedical application. *Chem Rev* 115:11669–11717
- Xu Q, Zhang Y, Tang B, Zhang C-Y (2016) Multicolor quantum dot-based chemical nose for rapid and array-free differentiation of multiple proteins. *Anal Chem* 88:2051–2058
- Wang L-J, Ma F, Tang B, Zhang C-Y (2016) Base-excision-repair-induced construction of a single quantum-dot-based sensor for sensitive detection of DNA glycosylase activity. *Anal Chem* 88:7523–7529
- Ma F, Li Y, Tang B, Zhang C-Y (2016) Fluorescent biosensors based on single-molecule counting. *Acc Chem Res* 49:1722–1730
- Zhou L, Gao C, Xu W (2010) Simultaneous photoluminescence import and mechanical enhancement of polymer films using silica-hybridized quantum dots. *J Mater Chem* 20:5675–5681
- Zhou L, Gao C, Hu X, Xu W (2010) One-pot large-scale synthesis of robust ultrafine silica-hybridized CdTe quantum dots. *ACS Appl Mater Interfaces* 2: 1211–1219
- Zhou L, Gao C, Xu W, Wang X, Xu Y (2009) Biomacromolecules, enhanced biocompatibility and biostability of CdTe quantum dots by facile surface-initiated dendritic polymerization. *Biomacromolecules* 10:1865–1874

15. Archana J, Navaneethan M, Hayakawa Y, Ponnusamy S, Muthamizhchelvan C (2012) Effects of multiple organic ligands on size uniformity and optical properties of ZnSe quantum dots. *Mater Res Bull* 47:1892–1897
16. Yu D, Du K, Zhang J, Wang F, Chen L, Zhao M, Bian J, Feng Y, Jiao Y (2014) Composition-tunable nonlinear optical properties of ternary $\text{CdSe}_x\text{S}_{1-x}$ ($x = 0-1$) alloy quantum dots. *New J Chem* 38:5081–5086
17. Bailey RE, Nie S (2003) Alloyed semiconductor quantum dots: tuning the optical properties without changing the particle size. *J Am Chem Soc* 125: 7100–7106
18. Zhong X, Feng Y, Knoll W, Han M (2003) Alloyed $\text{Zn}_x\text{Cd}_{1-x}\text{S}$ nanocrystals with highly narrow luminescence spectral width. *J Am Chem Soc* 125:13559–13563
19. Wang L, Cao L, Su G, Liu W, Xia C, Zhou H (2013) Preparation and characterization of water-soluble ZnSe:Cu/ZnS core/shell quantum dots. *Appl Surf Sci* 280:673–678
20. Regulacio MD, Han M-Y (2010) Composition-tunable alloyed semiconductor nanocrystals. *Acc Chem Res* 43:621–630
21. Adegoke O, Nyokong T, Forbes PBC (2015) Structural and optical properties of alloyed quaternary CdSeTeS core and CdSeTeS/ZnS core-shell quantum dots. *J Alloys Compd* 645:443–449
22. Yakoubi A, Chaabane TB, Aboulaich A, Mahiou R, Balan L, Medjahdi G, Schneider R (2016) Aqueous synthesis of Cu-doped CdZnS quantum dots with controlled and efficient photoluminescence. *J Lumin* 175: 193–202
23. S. Singh, Y. M. Sabri, D. Jampaiah, P. R. Selvakannan, A. Nafady, A. Esmailzadeh Kandjani, S. K. Bhargava, Easy, one-step synthesis of CdTe quantum dots via microwave irradiation for fingerprinting application, *Mater. Res. Bull.* (2017), in press.
24. Zhong XH, Han MY, Dong ZL, White TJ, Knoll W (2003) Composition-tunable $\text{Zn}_x\text{Cd}_{1-x}\text{Se}$ nanocrystals with high luminescence and stability. *J Am Chem Soc* 125:8589–8594
25. Yin Y, Alivisatos AP (2005) Colloidal nanocrystal synthesis and the organic–inorganic interface. *Nature* 437:664–670
26. Eaton DF (1988) Reference materials for fluorescence measurement. *Pure & Appl Chem* 60:1107–1114
27. Schneider CA, Rasband WS, Eliceiri KW (2012) NIH Image to ImageJ: 25 years of image analysis. *Nat Methods* 9:671–675
28. Rajeshwar K, de Tacconi NR, Chenthamarakshan CR (2001) Semiconductor-based composite materials: preparation, properties, and performance. *Chem Mater* 13:2765–2782
29. Tongay S, Suh J, Ataca C, Fan W, Luce A, Kang JS, Liu J, Ko C, Raghunathanan R, Zhou J, Ogletree F, Li J, Grossman JC, Wu J (2013) Defects activated photoluminescence in two-dimensional semiconductors: interplay between bound, charged, and free excitons. *Sci Rep* 3:2657
30. Veamatahau A, Jiang B, Seifert T, Makuta S, Latham K, Kanehara M, Teranishid T, Tachibana Y (2015) Origin of surface trap states in CdS quantum dots: relationship between size dependent photoluminescence and sulfur vacancy trap states. *Phys Chem Chem Phys* 17:2850–2858
31. Mansur HS (2010) Quantum dots and nanocomposites. *Wiley Interdiscip Rev Nanomed Nanobiotechnol* 2:113–129
32. Qian H, Li L, Ren J (2005) One-step and rapid synthesis of high quality alloyed quantum dots (CdSe-CdS) in aqueous phase by microwave irradiation with controllable temperature. *Mater Res Bull* 40:1726–1736
33. Osman MA, Othman AA, El-Said WA, Abd-Elrahim AG, Abu-sehly AA (2016) Thermal annealing and UV irradiation effects on structure, morphology, photoluminescence and optical absorption spectra of EDTA-capped ZnS nanoparticles. *J Phys D Appl Phys* 49:055304
34. Chen R, Li D, Liu B, Peng Z, Gurzadyan GG, Xiong O, Sun H (2010) Optical and excitonic properties of crystalline ZnS nanowires: toward efficient ultraviolet emission at room temperature. *Nano Lett* 10:4956–4961
35. Wageh S, Ling ZS, Xu-Rong X (2003) Growth and optical properties of colloidal ZnS nanoparticles. *J Cryst Growth* 255:332–337
36. Becker WG, Bard AJ (1983) Photoluminescence and photoinduced oxygen adsorption of colloidal zinc sulfide dispersions. *J Phys Chem* 87:4888–4893
37. Denzler D, Olschewski M, Sattler K (1998) Luminescence studies of localized gap states in colloidal ZnS nanocrystals. *J Appl Phys* 84:2841–2845
38. Uskokovic V (2008) Composites comprising cholesterol and carboxymethyl cellulose. *Colloids Surf, B* 61:250–261
39. Denton AR, Ashcroft NW (1991) Vegard's law. *Phys Rev A* 43:3161–3164
40. Vegard LZ (1921) Die konstitution der mischkristalle und die raumfüllung der atome. *Physik* 5:17–26
41. Brus LE (1984) Electron–electron and electron–hole interactions in small semiconductor crystallites: the size dependence of the lowest excited electronic state. *J Chem Phys* 80:4403–4409
42. Kumar H, Barman PB, Singh RR (2015) Effect of size and shell: enhanced optical and surface properties of CdS, ZnS and CdS/ZnS quantum dots. *Phys E* 67:168–177
43. Gao F (2011) Effects of quantum confinement and shape on band gap of core/shell quantum dots and nanowires. *Appl Phys Lett* 98:193105
44. Gao F (2010) A chemical bond theory of quantum size effects of semiconductor clusters. *Inorg Chem* 49:10409–10414
45. Gao L, Gao F (2013) Band gap prediction for composition-tunable alloyed semiconductor nanocrystals. *Appl Phys Lett* 103:053101
46. Egerton RF (2011) Electron energy loss spectroscopy in the electron microscope, 3rd edn. Springer, New York
47. Egerton RF (2009) Electron energy-loss spectroscopy in the TEM. *Rep Prog Phys* 72:016502
48. Baer DR, Engelhard MH (2010) XPS analysis of nanostructured materials and biological surfaces. *J Electron Spectrosc Relat Phenom* 178–179:415–432
49. Moulder JF, Stickle WF, Sobol PE, Bomben KD (1992) Handbook of X-ray photoelectron spectroscopy. Perkin-Elmer Corporation, Eden Prairie
50. Zorn G, Dave SR, Weidner T, Gao X, Castner DG (2016) Direct characterization of polymer encapsulated CdSe/CdS/ZnS quantum dots. *Surf Sci* 648:339–344
51. Barreca D, Gasparotto A, Maragno C, Tondello E, Spalding TR (2002) Analysis of nanocrystalline ZnS thin films by XPS. *Surf Sci Spectra* 9:51–64
52. López MC, Espinos JP, Martín F, Leinen D, Ramos-Barrado JR (2008) Growth of ZnS thin films obtained by chemical spray pyrolysis: the influence of precursors. *J Cryst Growth* 285:66–75
53. Ghazzal MN, Wojcieszak R, Raj G, Gaigneaux EM (2014) Study of mesoporous CdS-quantum-dot-sensitized TiO_2 films by using X-ray photoelectron spectroscopy and AFM. *Beilstein J Nanotechnol* 5:68–76
54. Mansur AAP, Saliba JB, Mansur HS (2013) Surface modified fluorescent quantum dots with neurotransmitter ligands for potential targeting of cell signaling applications. *Colloids Surf, B* 111:60–70
55. Ramanery FP, Mansur AAP, Borsagli FGLM, Mansur HS (2014) Green and facile synthesis of water-soluble ZnS quantum dots nanohybrids using chitosan derivative ligands. *J Nanopart Res* 16:2504
56. Mansur HS, Mansur AAPM, Curti E, de Almeida MV (2013) Functionalized-chitosan/quantum dots nano-hybrids for nanomedicine applications: towards biolabeling and biosorbing phosphate metabolites. *J Mater Chem B* 1:1696–1711
57. Mansur HS, Mansur AAPM, Curti E, de Almeida MV (2012) Bioconjugation of quantum-dots with chitosan and N, N, N-trimethyl chitosan. *Carbohydr Polym* 90:189–196
58. Irving H, Williams RJP (1953) The stability of transition-metal complexes. *J Chem Soc* 1953:3192–3210
59. Mellor DP, Maley L (1947) Stability constants of internal complexes. *Nature* 159:370–370
60. Reiss P, Protière M, Liang L (2009) Core/shell semiconductor nanocrystals. *Small* 5:154–168
61. Li Y, Zhong H, Li R, Zhou Y, Yang C, Li Y (2006) High-yield fabrication and electrochemical characterization of tetrapodal CdSe, CdTe, and $\text{CdSe}_x\text{Te}_{1-x}$ nanocrystals. *Adv Funct Mater* 16:1705–1716
62. H.S. Mansur, A.A.P. Mansur, A.A.P., A. Soriano-Araujo, Z.I.P. Lobato, Beyond biocompatibility: an approach for the synthesis of ZnS quantum dot-chitosan nano-immunoconjugates for cancer diagnosis, *Green Chem.* 17 (2015) 1820–1830
63. Mansur AAP, Mansur HS, de Carvalho SM, Lobato ZIP, Guedes MI, Leite MF (2016) Surface biofunctionalized CdS and ZnS quantum dot conjugates for nanomedicine and oncology: To be or not to be nanotoxic? *Int J Nanomedicine* 11:4669–4690
64. Chen X, Rangaiah GP, Zhao XS (2014) Photocatalytic degradation of methylene blue by titanium dioxide: Experimental and modeling study. *Ind Eng Chem Res* 53:14641–14649
65. Mansur AAP, Mansur HS, Ramanery FP, Oliveira LC, Souza PP (2014) “Green” colloidal ZnS quantum dots/chitosan nano-photocatalysts for advanced oxidation processes: study of the photodegradation of organic dye pollutants. *Appl Catal B* 158–159:269–279
66. Punnoose A, Dodge K, Rasmussen JW, Chess J, Wingett D, Anders C (2014) Cytotoxicity of ZnO nanoparticles can be tailored by modifying their surface structure: a green chemistry approach for safer nanomaterials. *ACS Sustainable Chem Eng* 2:1666–1673

67. Manner VW, Koposov AY, Szymanski P, Klimov VI, Sykora M (2012) Role of solvent–oxygen ion pairs in photooxidation of CdSe nanocrystal quantum dots. *ACS Nano* 6:2371–2377
68. W.G.J.H.M. van Sark, P.L.T.M. Frederix, D.J. Van den Heuvel, H.C. Gerritsen, A.A. Bol, J.N.J. van Lingen, C.M. Donegá, A. Meijerink, Photooxidation and photobleaching of single CdSe/ZnS quantum dots probed by room-temperature time-resolved spectroscopy, *J. Phys. Chem. B* 105 (2001) 8281–8284.

Submit your manuscript to a SpringerOpen[®] journal and benefit from:

- Convenient online submission
- Rigorous peer review
- Open access: articles freely available online
- High visibility within the field
- Retaining the copyright to your article

Submit your next manuscript at ► [springeropen.com](https://www.springeropen.com)
